Received: 22 June 2023 | Revised: 5 September 2023 | Accepted: 6 September 2023

DOI: 10.1002/pamm.202300033

RESEARCH ARTICLE

Peridynamic framework to model additive manufacturing processes

Jan-Timo Hesse | **Christian Willberg** | **Robert Hein** | **Felix Winkelmann**

German Aerospace Center, Institute of Lightweight Systems, Braunschweig, Germany

Correspondence
Jan-Timo Hesse, German Aerospace Center, Institute of Lightweight Systems, Lilienthalplatz 7, 38108 Braunschweig, Germany.
Email: jan-timo.hesse@dlr.de

Abstract

This paper introduces a novel framework for analyzing additive manufacturing processes. By employing a peridynamic mesh-free implementation, it overcomes certain limitations encountered with finite element-based approaches in regard to defects and fractures. The framework includes the implementation of thermodynamical material behavior and a novel boundary detection algorithm, as the outer surface area will undergo changes during the manufacturing process. The proposed methods are thoroughly validated, and a comprehensive example is provided as a demonstration.

1 | INTRODUCTION

Additive manufacturing allows the problem-specific production of parts. It is widely used to create small batches or prototypes [1]. Similar to other manufacturing processes [2], thermal effects influence the structural behavior of the resulting parts. However, a major challenge arises because the material used is created during the process, making it difficult to conduct representative testing in advance. Additionally, residual stresses resulting from the manufacturing process and defects are crucial aspects to consider. To simulate such effects, we have developed a Peridynamic framework.

Peridynamics, introduced by Stuart Silling in the early 2000s, has undergone continuous development since then. One of its main advantages is the absence of singularities, in the region of damage, as typically observed in classical continuum mechanics [3]. This is achieved through an integral description of the conservation of momentum. However, it is necessary to define an integration domain, which is a drawback of the method.

To predict failure in a thick adhesive layer and simulate crack propagation in isotropic materials, it is essential to have a simulating material model. Such a model has already been implemented and verified for the ordinary state-based formulation [4, 5]. Furthermore, this methodology has been applied at the microscale to study more complex phenomena [6]. However, Rädel et al. [7] showed that the convergence of the ordinary state-based formulation is significantly worse compared to the so-called correspondence formulation. Considering the increasing size and complexity of the models to be computed, the correspondence formulation offers more flexibility in material modeling compared to the ordinary-state based formulation, and therefore, it is utilized in this paper.

2 | PERIDYNAMIC MODELING

2.1 | Mechanical model

The paper follows the assumptions and notations from Silling et al. [3]. Within the neighborhood, compare Figure 1, $\mathcal{H}$, with the volume $V_{\mathbf{x}}$, defined by a spherical domain the horizon δ, the force volume density state $\underline{\mathbf{T}}$ for the bond interaction

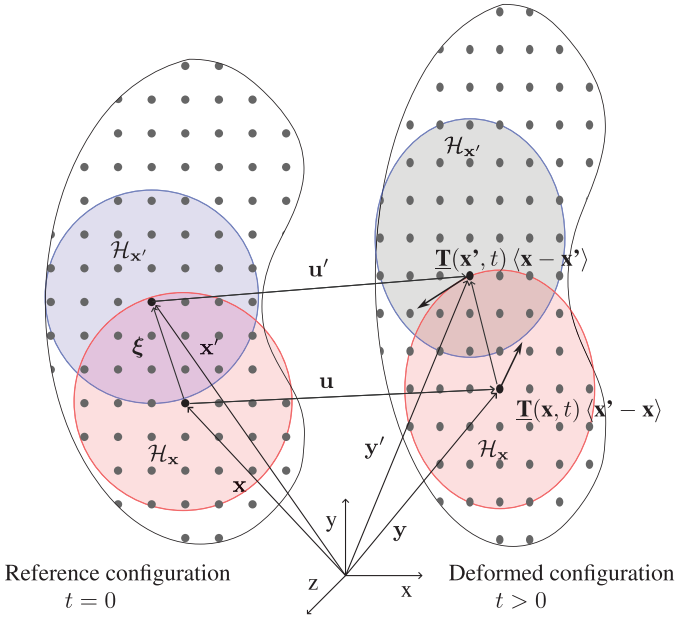

FIGURE 1 Deformation and interaction of material points $\mathbf{x}$ and $\mathbf{x}'$ in the non-ordinary state-based theory and their respective neighborhoods $\mathcal{H}_{\mathbf{x}}$ and $\mathcal{H}_{\mathbf{x}'}$.

between the positions $\mathbf{x}$ and $\mathbf{x}'$ is defined as the integral balance of momentum

$$\int_{\mathcal{H}} (\underline{\mathbf{T}}(\mathbf{x}, t)\langle \mathbf{x}' - \mathbf{x} \rangle - \underline{\mathbf{T}}(\mathbf{x}', t)\langle \mathbf{x} - \mathbf{x}' \rangle) dV_{\mathbf{x}} + \mathbf{b} = \rho \ddot{\mathbf{u}}. \tag{1}$$

Three variations of the peridynamic model are currently being used, the bond-based, the ordinary state-based and the non-ordinary state-based formulation. In this order, flexibility increases, but so does the complexity of the formulations.

A special formulation of the non-ordinary state-based model was introduced by Silling et al. [3] in 2007. This so-called "correspondence" formulation defines an integral non-local deformation gradient

$$\mathbf{F} = \left[\int_{\mathcal{H}} \underline{\omega}\langle \boldsymbol{\xi} \rangle \underline{\mathbf{Y}}\langle \boldsymbol{\xi} \rangle \otimes \underline{\mathbf{X}}\langle \boldsymbol{\xi} \rangle dV_{\mathbf{x}} \boldsymbol{\xi} \right] \cdot \mathbf{K}^{-1} \tag{2}$$

to calculate the bond force vector density states, where

$$\mathbf{K} = \int_{\mathcal{H}} \underline{\omega}\langle \boldsymbol{\xi} \rangle \underline{\mathbf{X}}\langle \boldsymbol{\xi} \rangle \otimes \underline{\mathbf{X}}\langle \boldsymbol{\xi} \rangle dV_{\mathbf{x}} \tag{3}$$

is the shape tensor with $V_{\mathbf{x}}$ defined as the neighborhood volume. For each bond $\boldsymbol{\xi} = \mathbf{x}' - \mathbf{x}$ an influence function $\underline{\omega}\langle \boldsymbol{\xi} \rangle$, an undeformed vector state $\underline{\mathbf{X}}\langle \boldsymbol{\xi} \rangle$ and a deformed vector state $\underline{\mathbf{Y}}\langle \boldsymbol{\xi} \rangle$ is defined. The shape tensor has to be positive definite and symmetric. The advantage of using the non-local deformation gradient is, that classical continuum mechanical models can be used in Peridynamics. The peridynamic force density vector state is thus

$$\underline{\mathbf{T}}\langle \boldsymbol{\xi} \rangle = \underline{\omega}\langle \boldsymbol{\xi} \rangle \mathbf{P}\mathbf{K}^{-1} \boldsymbol{\xi}\,. \tag{4}$$

The Piola-Kirchhoff stress tensor with respect to an orthonormal basis can be determined as

$$\mathbf{P} = \det \mathbf{F} \boldsymbol{\sigma} \mathbf{F}^{-1}\,. \tag{5}$$

2.2 | Thermal flux

The mechanical response due to temperature is included in the peridynamic model. However, the heat flux must be included as well. The following derivation is based on refs. [8, 9]. Under the assumption that mechanical deformations do not change the temperature, the thermodynamical equilibrium equation can be studied separately to Equation (1).

$$\rho C_v \dot{\tau} = \int_{\mathcal{H}} (\underline{h}(\mathbf{x}, t)\langle \boldsymbol{\xi} \rangle - \underline{h}(\mathbf{x}', t)\langle \boldsymbol{\xi}' \rangle) dV_{\mathbf{x}} + S_i \tag{6}$$

In contrast to Equation (1), which is a second-order differential equation, this equation is first-order, simplifying the numerical solving process. The parameters include ρ the mass density, C_v the specific heat capacity, $\dot{\tau}$ the temperature gradient in time, $dV_{\mathbf{x}}$ the volume and S_i the heat sink or heat source. The heat flux of a bond is defined as

$$\underline{h}(\mathbf{x}, t)\langle \boldsymbol{\xi} \rangle = \mathbf{q}^T \mathbf{K}^{-1}(\mathbf{x}) \boldsymbol{\xi} \tag{7}$$

with $\mathbf{q}$ as classical heat flux and $\mathbf{K}$ as the shape tensor defined in Equation (3). It follows

$$\nabla \cdot \mathbf{q} = \int_{\mathcal{H}} \left[\mathbf{q}(\mathbf{x}')^T \mathbf{K}^{-1}(\mathbf{x}') + \mathbf{q}(\mathbf{x})^T \mathbf{K}^{-1}(\mathbf{x}) \right] \boldsymbol{\xi} dV_{\mathbf{x}} \tag{8}$$

which can be derived utilizing the spatial gradient of the temperature $\nabla \tau$ as

$$\mathbf{q} = -\boldsymbol{\lambda} \nabla \tau. \tag{9}$$

$\boldsymbol{\lambda}$ is the 3×3 matrix of thermal conductivity, typically it is a diagonal matrix. Following [8] the spatial temperature gradient $\nabla \tau$ can be derived as

$$\nabla \tau = \mathbf{K}^{-1} \int_{\mathcal{H}} \left[\tau(\mathbf{x}') - \tau(\mathbf{x}) \right] \boldsymbol{\xi} \underline{\omega} \langle \boldsymbol{\xi} \rangle dV_{\mathbf{x}} \tag{10}$$

The numerical solving process is then

$$\rho C_v \frac{\tau^{t+dt} - \tau^t}{dt} = \nabla \mathbf{q} + S_i \tag{11}$$

$$\tau^{t+dt} = dt \frac{\nabla \mathbf{q} + S_i}{\rho C_v} + \tau^t \tag{12}$$

2.3 | Heat transfer to environment

Following [10, 11] the heat volumetric density at the surface for an assigned heat flux normal to the surface q_{bc} is

$$S_i = \frac{q_{bc}}{\Delta} \tag{13}$$

where Δ can be set to dx. Thereby, q_{bc} is

$$q_{bc} = \kappa(\tau - \tau_{env}) \tag{14}$$

where κ is the heat convection coefficient between solid and environment, and τ_{env} the environmental temperature. For a mesh-free model, the question arises: how the outer surface and the corresponded surface can be identified? For the outer surface the peridynamic neighborhood $\mathcal{H}$ is utilized. It is assumed that is circle for 2D and a sphere for 3D. Therefore, the

following criteria has to be fulfilled for 2D

$$V_{2D} = 2\pi\delta^2 h \geq \int_{\mathcal{H}} dV \tag{15}$$

and 3D

$$V_{3D} = \frac{4}{3}\pi\delta^3 \geq \int_{\mathcal{H}} dV \tag{16}$$

Each point, which is next to the surface will have less volume represented than the discrete material points. Defining a limit value

$$f_{limit} \leq V_{specific} = \frac{\int_{\mathcal{H}} dV}{V_{2D\,or\,3D}} \tag{17}$$

allows an easy identification of surface nodes i during the printing process. Combining Equations (12) and (13) allows the calculation of change in temperature for these nodes i as

$$\tau_i^{t+dt} = dt \frac{\nabla \mathbf{q}_i + \frac{\kappa(\tau_i^t - \tau_{env})}{dx}}{(\rho C_v)_i} + \tau_i^t . \tag{18}$$

The minimum time step for the explicit time integration of the temperature field, to obtain a stable solution is given by

$$\Delta t < \min\left(\frac{(\rho C_v)_i}{\sum_{j=1}^{N} \frac{\max(\mathrm{eig}(\lambda))}{|\xi_{ij}|} V_j} \right) \tag{19}$$

with N the number of neighbors of point i [12].

2.4 | Additive model

The additive model is realized by including a print path. This path gives each node a time stamp $t_{activate}$. This time represents the position of the printer during the printing process. In order to activate bonds the influence function $\underline{\omega}\langle\boldsymbol{\xi}\rangle$ defined in Equations (4) and (10) is used. In the simplest case, presented here in the paper, $\underline{\omega}\langle\boldsymbol{\xi}\rangle$ is defined as

$$\underline{\omega}\langle\boldsymbol{\xi}\rangle \in \mathcal{H}_{\mathbf{x}} = \begin{cases} 0 & \text{for } t < t_{activate} \\ 1 & \text{for } t \geq t_{activate} \end{cases} \tag{20}$$

The printing temperature is included, utilizing the heat source S_i introduced in Equation (6). It must be noted that after activation in Equation (20) the bonds are not in a constant state. They can be deactivated due to damages as well. Numerically, this includes the bonds not being checked after activation.

3 | RESULTS

Conclusion

The verification shows that all models were implemented in a correct way. The errors compared to the reference solutions are low and can be reduced by using finer discretizations, if the spacial distribution is not sufficient (see Figures 2 and 3).

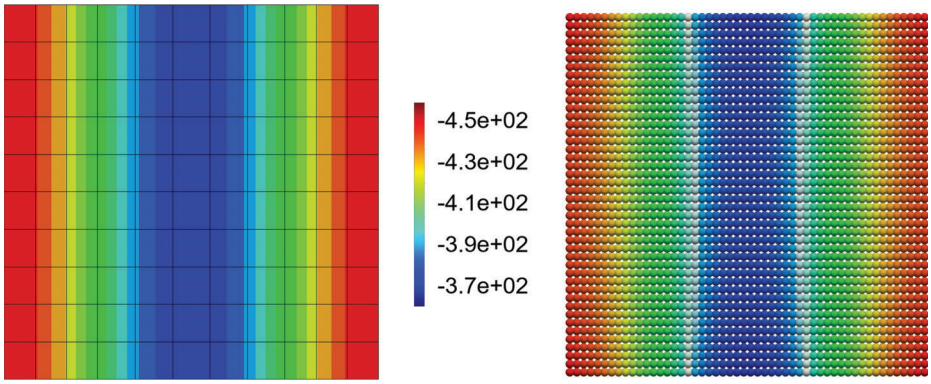

FIGURE 2 Geometry and discrete model for the verification of the cooling process based on heat flow.

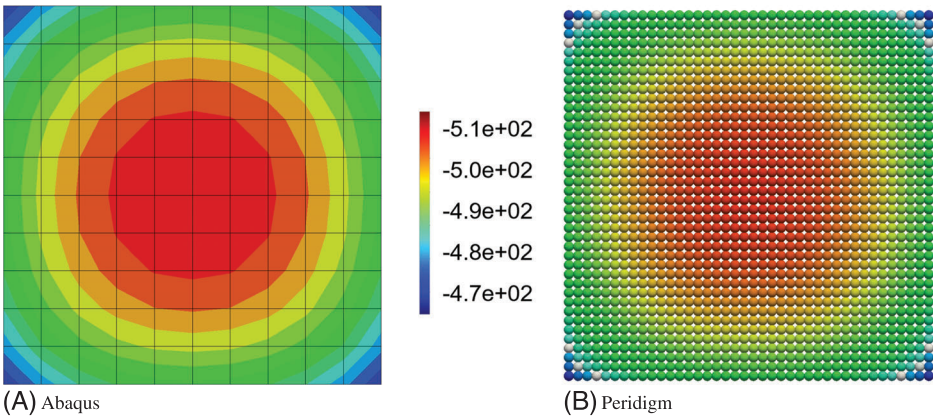

FIGURE 3 Geometry and discrete model for the verification of the cooling process based on heat convection.

4 | PRINTING

This section describes how the peridynamic mesh is generated based on the G-code and the corresponding CAD (computer-aided design) model.

4.1 | Printing process

To simulate the thermomechanical behavior of an additive material using Peridynamics, a geometric model is required. This entails a list of points, their corresponding volumes, and material properties for the mesh-free approximation. The process begins with the CAD model of the structure intended for printing. Typically, the printing process is controlled by the widely used G-code, a computer numerical control programming language. This code is derived from the CAD model using commercial software, and it describes the path and speed of the printing process. It is necessary to interpret and translate this numerical process information into the Peridynamic representation.

The following steps are involved in generating a discretized mesh:

- CAD to Peridynamic mesh conversion
- Extracting parameters from G-code
- Retrieving printing path from G-code
- Calculating node timing and orientation
- Identifying Peridynamic nodes within a bounding box along the printing path
- Assigning timing and orientation to mesh points
- Writing the converted mesh

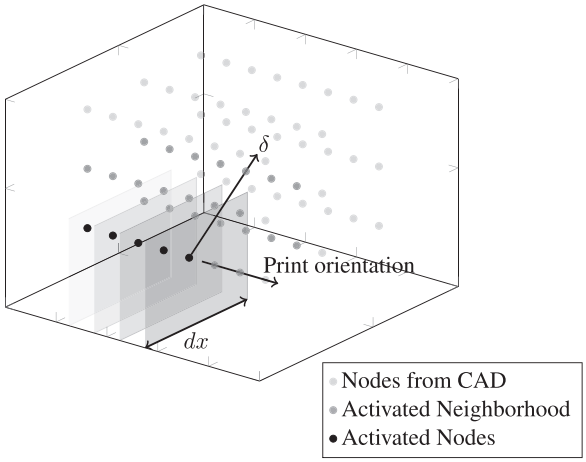

FIGURE 4 Conversion schema.

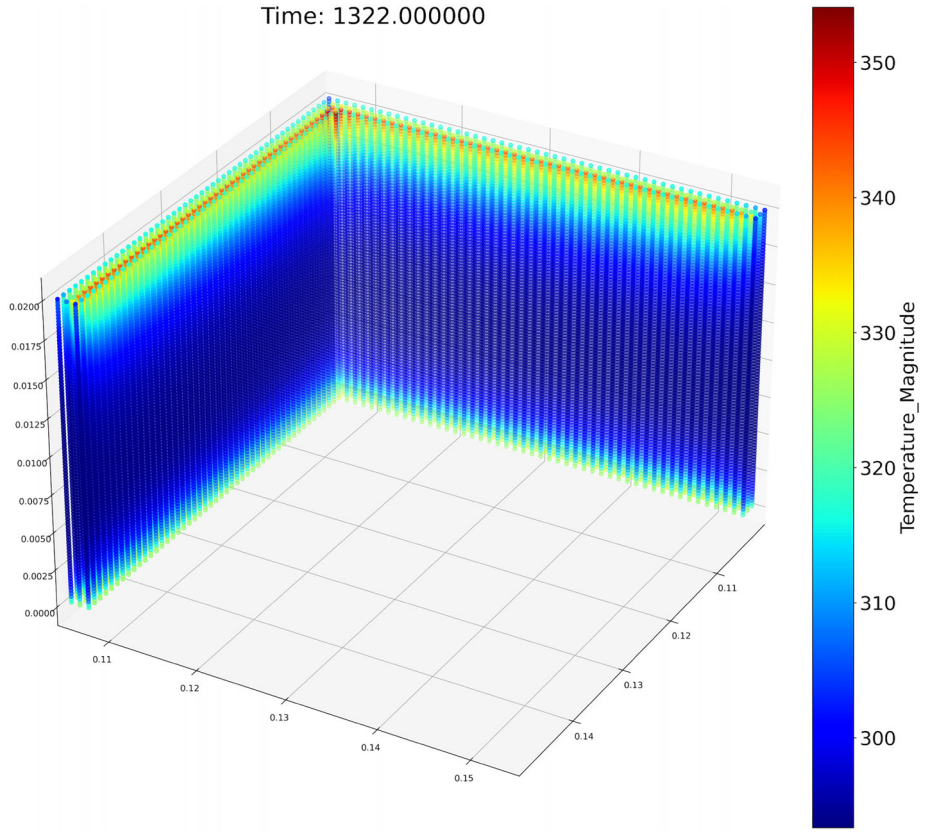

FIGURE 5 Peridynamic L-angle simulation results.

The first step involves discretizing the CAD model into a mesh of volume elements. The mesh-free material point-based Peridynamic mesh uses the center of gravity of each element as the position of the material point, with the element volume corresponding to the material point volume. For additive manufacturing, it is crucial to determine when regions become active.

Information regarding the printing path and processing speed is obtained from the G-code to determine the activation time and material orientation for the material points. Basic parameters such as nozzle width and layer height are also extracted from the G-code.

The printer's path, as described by the G-code, is extracted. The nozzle movement is mainly described by linear interpolations between fixed start and endpoints, with the corresponding velocity determined by the feed rate. Following the G-code path, the Peridynamic mesh is obtained. The maximum step width is defined by the minimum distance between

two material points in the Peridynamic mesh. Since the path is represented as a line, a bounding box is placed around the print path points to identify the material points that need to be activated. These points are assigned the corresponding printing time as the virtual printer reaches them. As depicted in Figure 4, every Peridynamic node intersected by the bounding box receives the appropriate printing time and orientation. This approach allows for arbitrary discretizations, as multiple points can be activated simultaneously.

If the assigned time-value of the nodes is reached by the peridynamic simulation time, the node and its neighborhood will be activated. Hence, we are able to simulate the temperature distribution of additive materials.

5 | CONCLUSION

This paper demonstrates the implementation and verification of thermodynamical material behavior, it also introduces a novel dynamic surface detection algorithm. By combining this algorithm with the printing time information from the G-code, we showcase the peridynamic framework's ability to simulate additive manufacturing processes. As a concrete example, Figure 5 illustrates the final temperature of a newly printed L-Angle probe.

Due to computational time, only the temperature distribution was calculated. For further research, the full thermo-elastic material behavior will need to be analyzed. Moreover, material effects that will occur, such as phase transitions, need to be implemented. This could be achieved with an existing User Material (UMAT) subroutine.

ACKNOWLEDGMENTS

Open access funding enabled and organized by Projekt DEAL.

ORCID

Jan-Timo Hesse https://orcid.org/0000-0002-3006-1520
Christian Willberg https://orcid.org/0000-0003-2433-9183

REFERENCES

1. Hartmann, P., Weißenfels, C., & Wriggers, P. (2021). A curing model for the numerical simulation within additive manufacturing of soft polymers using Peridynamics. *Computational Particle Mechanics*, *8*, 369–388.
2. Liebisch, M., Hein, R., & Wille, T. (2018). Probabilistic process simulation to predict process induced distortions of a composite frame. *CEAS Aeronautical Journal*, *9*, 545–556.
3. Silling, S. A., Epton, M., Weckner, O., Xu, J., & Askari, E. (2007). Peridynamic states and constitutive modeling. *Journal of Elasticity*, *88*, 151–184.
4. Foster, J. T., Silling, S. A., & Chen, W. (2011). An energy based failure criterion for use with Peridynamic states. *International Journal for Multiscale Computational Engineering*, *9*(6), 675–688.
5. Willberg, C., Wiedemann, L., & Rädel, M. (2019). A mode-dependent energy-based damage model for Peridynamics and its implementation. *Journal of Mechanics of Materials and Structures*, *14*(2), 193–217.
6. Rädel, M., Willberg, C., & Krause, D. (2019). Peridynamic analysis of fibre-matrix debond and matrix failure mechanisms in composites under transverse tensile load by an energy-based damage criterion. *Composites Part B: Engineering*, *158*, 18–27.
7. Rädel, M., Willberg, C., & Schmidt, J. (2017). Effect of discretization and stochastic material distribution on crack initiation in peridynamics. In *14th U.S. national congress on computational mechanics* USNCCM 14.
8. Brighenti, R., Zeleke, M. A., & Ageze, M. B. (2021). A review of Peridynamics (PD) theory of diffusion based problems. *Journal of Engineering*, *2021*, 20.
9. Xue, T., Zhang, X., & Tamma, K. K. (2018). A two-field state-based Peridynamic theory for thermal contact problems. *Journal of Computational Physics*, *374*, 1180–1195.
10. Gu, X., Zhang, Q., & Madenci, E. (2019). Refined bond-based Peridynamics for thermal diffusion. *Computer Methods in Applied Mechanics and Engineering*, *36*, 2557–2587.
11. Oterkus, S., Madenci, E., & Agwai, A. G. (2014). Peridynamic thermal diffusion. *Journal of Computational Physics*, *265*, 71–96.
12. Oterkus, S., Madenci, E., & Agwai, A. G. (2014). Fully coupled Peridynamic thermomechanics. *Journal of the Mechanics and Physics of Solids*, *64*, 1–23.

How to cite this article: Hesse, J.-T., Willberg, C., Hein, R., & Winkelmann, F. (2023). Peridynamic framework to model additive manufacturing processes. *Proceedings in Applied Mathematics and Mechanics*, e202300033. https://doi.org/10.1002/pamm.202300033